



HAL
open science

Nanocube epitaxy for the realisation of printable monocrystalline nanophotonic surfaces

Anna Capitaine, Beniamino Sciacca

► **To cite this version:**

Anna Capitaine, Beniamino Sciacca. Nanocube epitaxy for the realisation of printable monocrystalline nanophotonic surfaces. *Advanced Materials*, 2022, 10.1002/adma.202200364 . hal-03538271v2

HAL Id: hal-03538271

<https://hal.science/hal-03538271v2>

Submitted on 31 Mar 2022

HAL is a multi-disciplinary open access archive for the deposit and dissemination of scientific research documents, whether they are published or not. The documents may come from teaching and research institutions in France or abroad, or from public or private research centers.

L'archive ouverte pluridisciplinaire **HAL**, est destinée au dépôt et à la diffusion de documents scientifiques de niveau recherche, publiés ou non, émanant des établissements d'enseignement et de recherche français ou étrangers, des laboratoires publics ou privés.

Nanocube epitaxy for the realisation of printable monocrystalline nanophotonic surfaces

Anna Capitaine Beniamino Sciacca*

Aix Marseille Univ, CNRS, CINaM, AMUtech, Marseille, France
Campus de Luminy, 13288 Marseille (France)
Email Address: beniamino.sciacca@cnrs.fr

Keywords: *Nanocube epitaxy, Monocrystalline gold nanoantennas, Chemistry in-operando, Plasmonics*

Plasmonic nanoparticles of the highest quality can be obtained via colloidal synthesis at low-cost. Despite the strong potential for integration in nanophotonic devices, the geometry of colloidal plasmonic nanoparticles is mostly limited to that of Platonic solids. This is in stark contrast to nanostructures obtained by top-down methods, that offer unlimited capability for plasmon resonance engineering, but present poor material quality and have doubtful perspectives for scalability. Here, we introduce an approach that combines the best of the two worlds by transforming assemblies of single-crystal gold nanocube building blocks into continuous monocrystalline plasmonic nanostructures with an arbitrary shape, via epitaxy in solution at near ambient temperature. We used nanocube dimers as a nanoreactor model system to investigate the mechanism *in operando*, revealing competitive redox processes of oxidative etching at the nanocube corners and simultaneous heterogeneous nucleation at their surface, that ensure filling of the sub-nanometer gap in a self-limited manner. Applying this procedure to nanocube arrays assembled in a patterned polydimethylsiloxane (PDMS) substrate, we are able to obtain printable monocrystalline nanoantenna arrays that can be swiftly integrated in devices. This could lead to the implementation of low cost nanophotonic surfaces of the highest quality in industrial products.

1 Introduction

Controlling the geometry of individual nanostructures and their assembly into organized arrays, on a large area at low cost, is key to take nanophotonic and plasmonic devices from a laboratory scale to industrial products [1, 2, 3]. In particular, metal nanoparticles support surface plasmon resonances that are responsible for confining light to a dimension much smaller than the corresponding free-space wavelength and enable for large optical cross-sections [4, 5, 6, 7, 8, 9, 10]. As a result of this intense light confinement, the optical and electrical properties strongly depend on size, shape, material properties and dielectric environment. The unique features of plasmonic nanostructures has led to countless applications in various fields. As an example, supported on a substrate they have been proposed for surface-enhanced spectroscopy [11, 12, 13, 14], catalysis [15, 16, 17], sensing [18, 19, 14] and diverse photonic applications [20] that take advantage of the properties of individual nanoparticles [21] or of the collective resonances of phased arrays [8, 6, 22] to name a few.

Control on the nanoscale geometry is commonly achieved by patterning thin films via lithography techniques followed by evaporation and lift-off processes or etching [23]. Such top-down nanofabrication steps not only are expensive, time consuming and hardly scalable, but produce materials that are polycrystalline, have substantial surface roughness or present damages as a result of etching. On the contrary, material quality is of paramount importance to building high efficiency optoelectronic and nanophotonic devices [6, 24, 25, 26]. Therefore, monocrystalline materials are ideal constituents to reach ultimate performance. However, this requirement adds further fabrication complexity owing to an epitaxial growth step to form a thin film prior to nanostructuring. This substantially restricts the integration to layers that are lattice-matched and that can withstand high temperature, vacuum [24] and possibly wet lift-off steps[27].

Chemical syntheses on the other hand allow one to obtain high-quality colloidal nanoparticles, free of grain boundaries or stress that hamper electron conduction and weaken plasmon resonances [28, 24]. A variety of shapes (nanowires, nanocubes, nanoplates, nanoflowers, nanoprisms, etc...) can be achieved by tuning the synthesis parameters or by particle attachment [29], with extensive control of size and material composition. Nevertheless, gaining further control on the shape of nanocrystals beyond that of conventional Platonic solids, is crucial to introduce morphological anisotropy by design and tune the physicochemical properties to specific applications [30]. This hinders the realisation of nanophotonic surfaces having individual units

with an arbitrarily complex geometry, that is often needed in plasmonics, and therefore limits substantially their potential.

Here we lift this barrier and take advantage of solution processed nanomaterials (nanocubes) to fabricate extended 1D and 2D monocrystalline nanostructure arrays of arbitrary shape (at near ambient temperature) and print them to any substrate. Single-crystal nanocubes are ideal building blocks because they have the highest intrinsic material quality and they have a 4-fold rotational invariance. This ensures identical crystallographic orientation of adjacent units, that is crucial to transform a discontinuous assembly into a continuous monocrystalline nanostructure via nanocube epitaxy [31]. This makes solution synthesis a promising route towards the fabrication of low cost nanophotonic surfaces of highest quality.

A variety of materials used for optoelectronic applications can be synthesized as single-crystal nanocubes in solution, as for example Ag, Au, Cu, Al [32, 33, 34] (metals) Cu_2O , PbS , CsPbX_3 [35, 36, 37] (semiconductors) and BiFeO_3 , SrTiO_3 and CeO_2 [38, 39, 40] (dielectric), to name a few. Among them gold stands as an excellent candidate because it exhibits very good electrical and optical properties, and it is a prime choice in many plasmonic and nanophotonic devices [6, 41]. In addition, the excellent thermal and chemical stability enable to study nanocube epitaxy without interference from the environment, oxide layers or absorbed species.

First, we demonstrate that the strategy described above can be used as a general method to transform arbitrary assemblies of gold nanocubes (supported on a silicon substrate) into 1D and 2D monocrystalline nanostructures. This is enabled by the introduction of a novel approach of simultaneous oxidative dissolution and growth, that can also be used to control the faceting of the resulting continuous monocrystalline nanostructures by tuning few key parameters. Then, we show for the first time that by applying this procedure to nanocubes organized in polydimethylsiloxane (PDMS) via directed assembly, monocrystalline Au nanopatterns by design can then be transferred to virtually any kind of substrate. This paves the way for swift integration of nanophotonic surfaces of the highest quality in optical and optoelectronic devices and architectures that are incompatible with classic nanopatterning strategies such as perovskite layers. Finally, we extensively study the chemical framework for nanocube epitaxy with a set of controlled experiments *ex-situ* and *in operando* on a nanocube dimer model system. This provides with invaluable insights on the mechanism with atomic scale resolution.

2 Results and Discussions

2.1 Welding of adjacent nanocubes on silicon

Gold nanocubes (30 to 40-nm) are synthesized following the procedure earlier reported by Park *et al.* [28]. The solutions are highly monodisperse, and when dropcasted on a substrate nanocubes self-assemble face-to-face in a 2D closed-packed configuration, separated by a layer of adsorbed ligands (0.375 ± 0.076 nm) residual from the synthesis (Figure S1, Figure S14).

After deposition, nanocubes are extensively washed with solvents and sodium borohydride (NaBH_4) to remove the ligands (see experimental section) and obtain pristine surfaces separated by sub-nanometer gaps [42, 31]. This constitutes an ideal platform to study nanocube epitaxy, as the product can swiftly be characterized with scanning electron microscopy (SEM). If exposed to a solution containing a gold precursor (HAuCl_4) and a weak reductant (ascorbic acid), adjacent nanocubes grow and merge, producing continuous gold nanostructures (Figure S2). Unfortunately, reduction of AuCl_4^- in the bulk of the solution leads to homogeneous nucleation, causing contamination of the sample with small nanocrystals and inefficient use of reactants. We therefore explored the opportunity to achieve nanocube epitaxy in the absence of a reducing agent, so that AuCl_4^- ions can reach the nanocubes surface without being consumed in the bulk of the solution.

Figure 1 presents evidence of nanocube epitaxy at near ambient temperature, for 35 nm and 38 nm nanocubes (panel c and a, respectively) achieved using a solution of HAuCl_4 80 μM only. The sub-nanometer gaps are successfully filled, yielding to continuous 1D and 2D nanostructures whose geometry is directed by the position of the nanocubes prior to welding, with good shape and angle retention. The

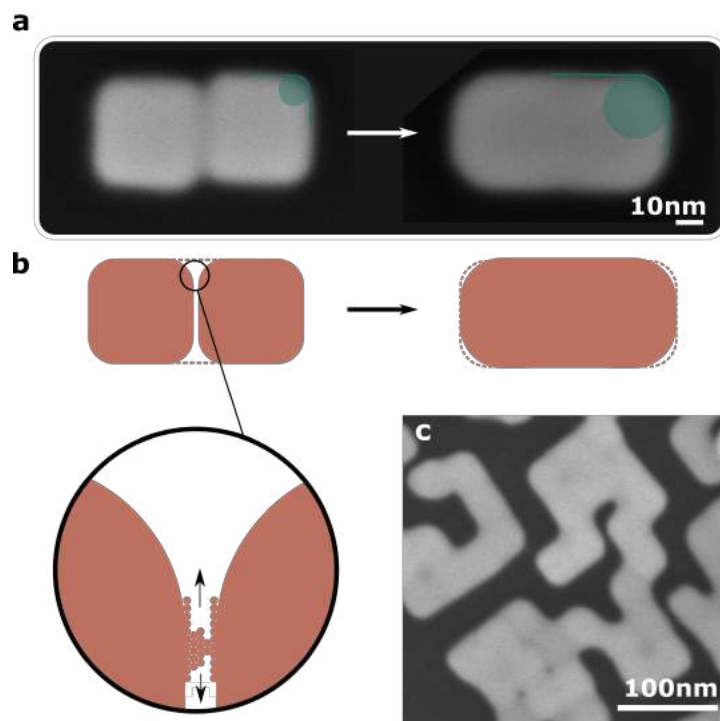


Figure 1: Epitaxial welding of gold nanocubes on silicon using a solution of HAuCl_4 only. a) SEM image of two 38-nm ligand-free nanocubes on silicon before (left) and after exposure to a $80\mu\text{M}$ HAuCl_4 solution at 40°C for 5 minutes (right); the green circles represent the radius of curvature. b) Schematic representation of the welding. c) SEM image of self-assembled 35-nm nanocubes after ligand removal and welding with a $80\mu\text{M}$ HAuCl_4 solution at 40°C for one second.

resulting 1D nanostructures (Figure 1a) are on average $\sim 10\%$ wider compared to the nanocubes before welding (from 35.5 ± 2.16 to 39.59 ± 3.37 nm and from 37.75 ± 1.22 nm to 42.73 ± 1.78 nm), whereas the length is unchanged (70 ± 0.68 nm for 35-nm nanocubes and 78.28 ± 2.98 nm for 38-nm nanocubes) (Figure S14). This is key to the realization of nanostructures that have an arbitrary geometry with control down to the nanometer scale. The radius of curvature increases after welding (see statistics in Figure S14), which is attributed to oxidative etching of the nanocube corners, and it is amplified as the HAuCl_4 concentration increases or when Cl^- ions are added to the solution (see next). Besides preventing homogeneous nucleation and avoiding sample contamination with small nanocrystals, we found that this strategy is robust, as it leads to successful welding over a wide range of HAuCl_4 concentration ($1\ \mu\text{M}$ - $10\ \text{mM}$), reaction temperature (room temperature (RT) - 80°C) and pH, with a time scale from less than a second (Figure 1c) to a few minutes, despite the fact that no reductant is introduced in the solution. A good compromise between fast kinetic and nanocube shape retention was found using $80\ \mu\text{M}$ HAuCl_4 at a temperature of 40°C . These conditions will be used as reference in this article when performing the welding on silicon, unless stated otherwise.

2.2 Printable monocrystalline nanoantenna arrays

Applying the welding procedure on gold nanocubes organized in arrays enables us to realize monocrystalline nanopatterned surfaces with extensive morphology control, that is especially important for plasmonics and nanophotonics. The low surface energy of PDMS makes it a convenient support for nanostructures self-assembly and growth, and ensures that those can be later released to virtually any substrate by contact printing (Figure 2a). Micro and nanoparticles can be assembled in nanostructured PDMS using capillary assembly [43, 44, 45, 46, 47]. Silicon masters were patterned using e-beam lithography and used to fabricate PDMS moulds with traps designed to accommodate a certain number of nanocubes in a given geometry. Using this technique we realized periodic arrays of 2, 3, 4, 5 and 8 nanocubes as a proof of concept (Figure 2b and S12), but there is no limit to the geometry that can be obtained.

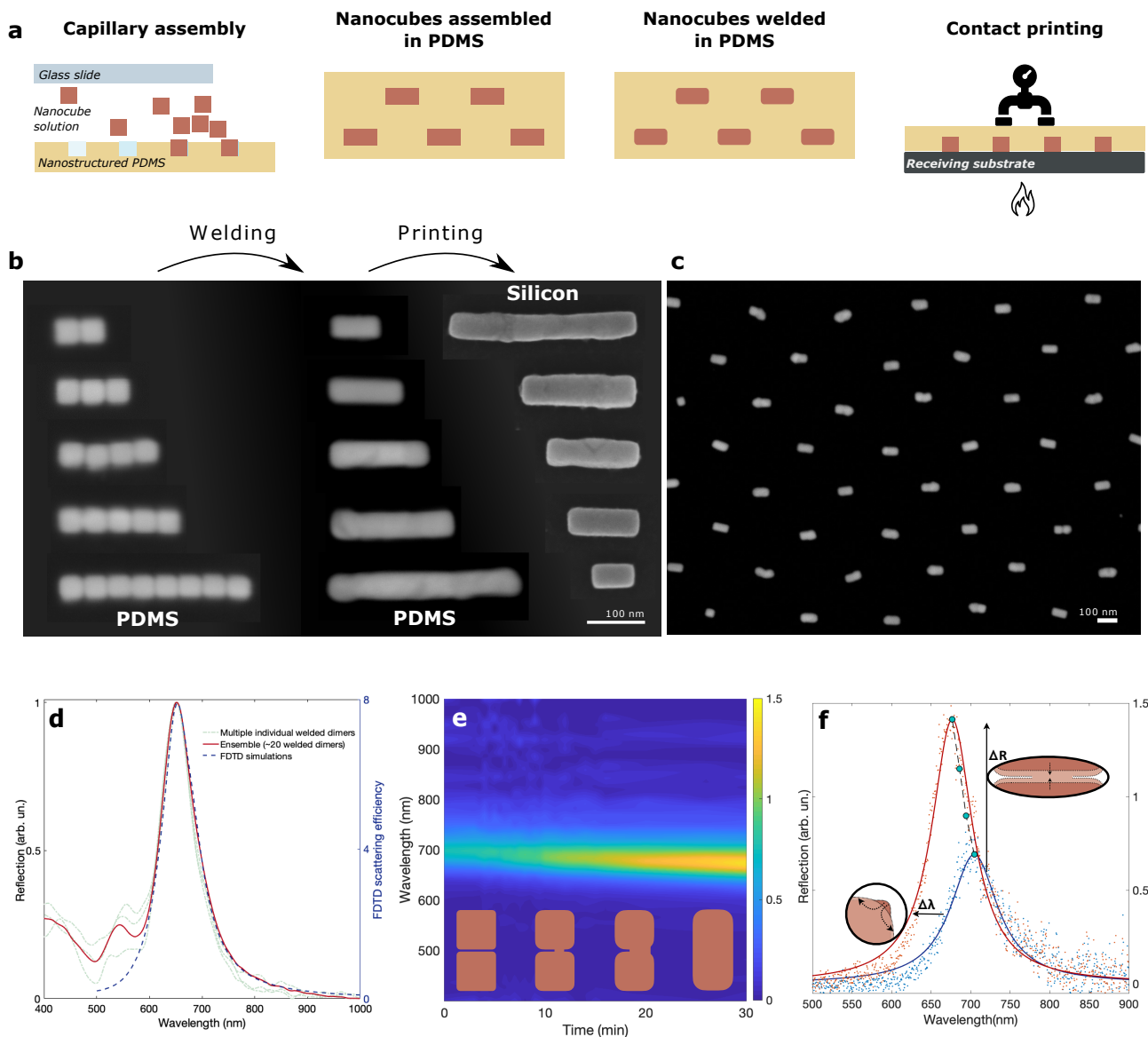


Figure 2: Realization of monocrystalline nanostructures by design on PDMS. a) Illustration of the process: capillary assembly in nanopatterned PDMS, nanocube epitaxy in solution and printing of monocrystalline nanostructures to any substrate. b) Collage of SEM images taken from large arrays made of 2, 3, 4, 5 and 8 nanocubes, showing 38 nm gold nanocubes assembled into 1D nanostructures of arbitrary length in PDMS before nanocube epitaxy (left image), after nanocube epitaxy in PDMS (middle image) and after printing to a silicon substrates (right image). c) SEM image of nanoantenna arrays on PDMS after nanocube epitaxy. d) Optical response (unpolarized light) of multiple individual nanoantennas (dotted line) and nanoantenna array (solid line) supported on PDMS, showing the intense dipolar longitudinal mode at 680 nm and the transverse mode at 550 nm. Realistic FDTD simulations of the nanoantenna array in PDMS (blue dashed line, polarisation parallel to the dimer long axis); the agreement with experimental data in terms of resonance position and full-width-half-max (FWHM) confirms the realisation of a material of the highest quality. e) Nanocube epitaxy on a model system *in operando*. An ensemble of ~ 40 dimers in an array configuration on PDMS (panel c) is probed during epitaxy performed at RT; inset: diagram illustrating the evolution of nanocube dimers into a continuous welded bar. f) Data in panel d at the beginning ($t = 0$ s) and at the end ($t = 30$ min) of nanocube epitaxy, and the corresponding Lorentzian fits (solid lines). The green dots represent the resonance position at intermediate times. The blue-shift, the increase in intensity of the dipolar mode and the narrowing of the linewidth testify changes of the system morphology at the atomic scale. The scale bar in SEM images is 100 nm.

The welding procedure using HAuCl_4 only optimized for nanocubes supported on a silicon substrate did not yield consistent results on different substrates, such as glass, Si_3N_4 or PDMS, most likely due to differences in surface chemistry and surface energy that impact the local reaction environment (more

detail in SI). Results on silicon revealed that two mechanisms were at play: oxidation of the nanocube corners and gold reduction at the surface. Slight modification of the welding procedure, by performing the reaction at pH 1 (to promote oxidation) and introducing micromolar concentrations of NaBr (to enhance (100) facets reactivity [48]) enabled gold nanocube epitaxy on all substrates, including PDMS, transforming the welding procedure developed on silicon into a general solution route towards continuous monocrystalline nanostructures of arbitrary shape (Figure 2b). Figure 2c illustrates a periodic array of gold nanoantennas (with an aspect ratio of 2) obtained via nanocube epitaxy on a PDMS substrate. The sample exhibits homogeneous welding and very good shape retention throughout the entire substrate (200 μm X 200 μm). The optical response of individual nanoantennas and of an ensemble are compared in Figure 2d. The reflection peak at 650 nm corresponds to the longitudinal dipolar mode. It is worth noting that (i) different individual dimers show approximately the same behaviour, (ii) the collective response of an ensemble of ~ 20 dimers is almost identical to that of individual dimers, (iii) the resonance linewidth and position are in extraordinary agreement with Finite Difference Time Domain (FDTD) simulations, indicating a material of the highest quality. This provides evidence that nanocube epitaxy enables the realisation of bottom-up nanophotonic surfaces, with an exquisite control of position and geometry of individual resonators (comparable to e-beam lithography), and a material quality superior to what can be achieved with metal evaporation, that is the standard approach in nanofabrication.

The regular geometry of the nanoantenna array constitutes an ideal platform to examine nanocube epitaxy *in operando*, permitting to probe simultaneously the optical response of a number of nanoreactors. The strong light confinement in plasmonic nanoparticle systems allows extraordinary sensitivity to their geometry and their environment [21]. Compared to other *in operando* techniques, such as liquid-phase TEM, optical approaches ensure minimal perturbation, that is especially important to study redox chemical reactions. We will show that this can be used to access information on nanocube epitaxy, with atomic resolution.

Figure 2e presents the kinetics of nanocube epitaxy, corresponding to the collective reflection of ~ 40 dimers nanoreactors supported on PDMS, starting from the exposure to the welding solution to complete epitaxy. The main features that can be evidenced in the kinetic response are illustrated in Figure 2f. At time $t = 0$, electron tunneling through the < 0.5 nm gap (see Figure S14) enables a dipolar response of the entire dimer via a charge transfer plasmon mode, as evidenced by the E_z field profile shown in Figure S16a. As welding takes place ($t > 0$) new adatoms from the nanocube corners and from the solution slowly fill the nanogap, eventually establishing a bridge between the isolated nanocubes. As the bridge widens, electron tunneling is superseded by electron conduction through the lattice (see Figure S16b). As a consequence of the larger electron current in the gap, the scattering cross-section of the dipolar mode increases. This leads to an increase of the array reflectance in the far-field, as observed in Figure 2e,f. The blue-shift (~ 25 nm) of the dipolar mode is associated with the rounding of the nanocube corners (from $r \sim 5$ nm to $r \sim 9$ nm) and the increase in width (from $w \sim 38$ nm to $w \sim 43$ nm) during welding. The impact of the morphology of the welded dimer on the mode resonance is simulated in Figure S17a,b (w or r only) and Figure S17c (w and r combined). Figure S18 compares the FDTD response of a dimer array before welding with the corresponding array after welding, taking into consideration the change in morphology. The main features observed experimentally can be reproduced almost quantitatively. Note that the morphology of the interfaces has a strong impact on the optical response of dimers as they merge into a continuous nanoscale object [49, 50]. These data are the signature of changes of the atomic arrangement inside a sub-nanometer gap with unprecedented resolution, and suggest that the processes of oxidation, growth and welding take place simultaneously.

Finally, such monocrystalline nanophotonic surface can be transferred from PDMS to other substrates for integration in optoelectronic devices, or for further characterisation. Figure 2b, shows nanoantennas of different lengths deposited from PDMS to silicon. During this process, the PDMS stamp is pressed against a receiving substrate, and the nanostructures are released due to the larger adhesion forces. It is worth noticing that the bottom surface of the nanoantennas, initially in contact with PDMS, also exhibit a continuous, gap-free surface. The nanoantenna arrays were printed from PDMS to a Si_3N_4 membrane for high-resolution TEM (HRTEM) characterization. HRTEM images on different locations and electron

diffraction on the whole nanostructure are presented in Figure 3. These provide evidence (i) for a perfect crystallographic alignment of the two nanocubes at the time of assembly, (ii) for epitaxy between individual building blocks, and (iii) that the junction is filled in its entirety yielding gap-free monocrystalline nanostructures. In addition, we noticed that epitaxy can be achieved also in the presence of non-cubic nanoparticles (defects) with a different crystallographic orientation, and result in the formation of a grain boundary (Figure S13). This could promote grain boundaries engineering and trigger new material-by-design approaches [51, 52].

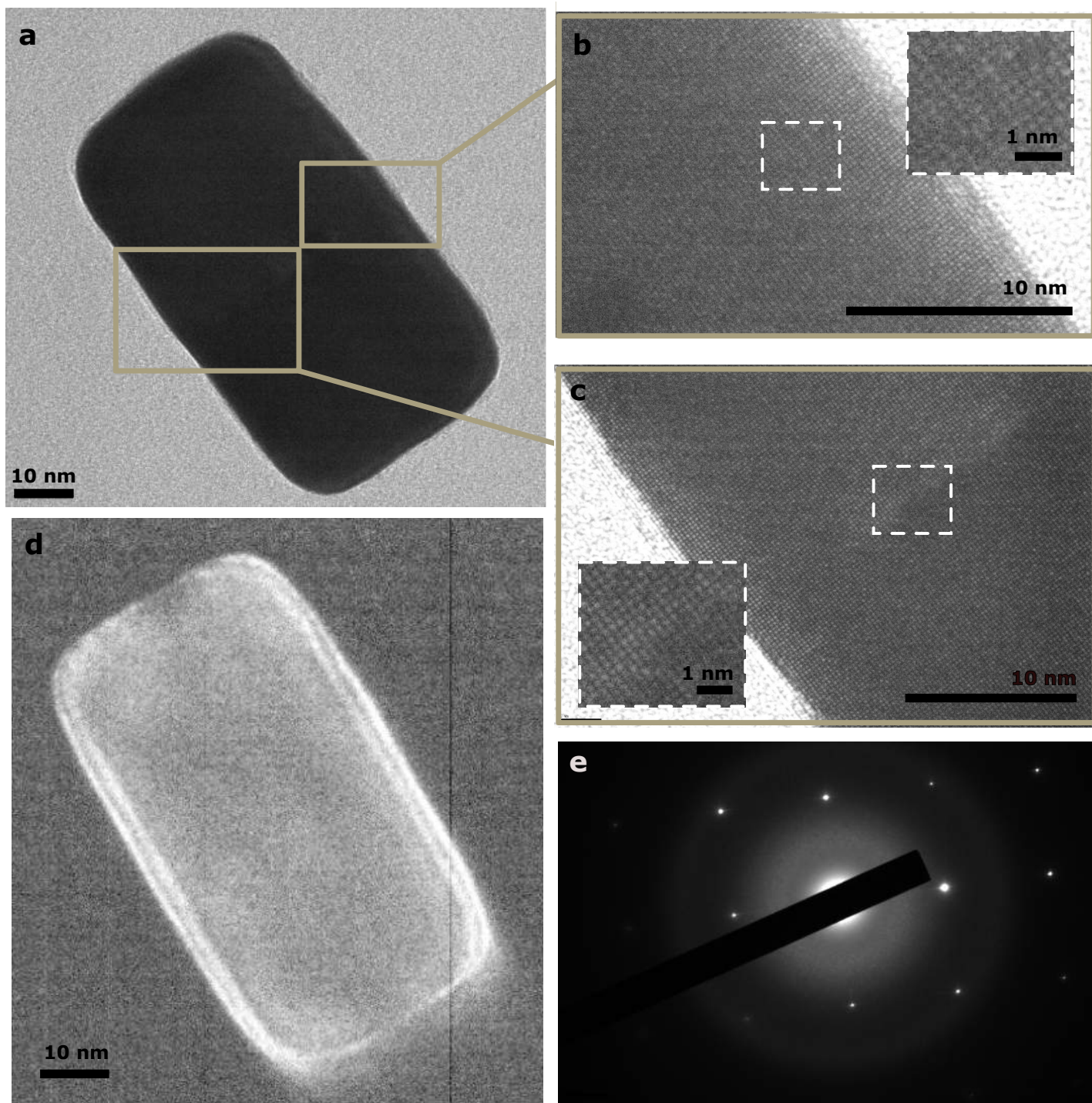


Figure 3: TEM characterization of the dimer arrays after epitaxy. a) Bright-field image. b), c) HRTEM showing a continuous gap-free material at the approximate location of where the junction between two nanocubes was before welding. d) Dark-field image showing no contrast at the junction. e) Electron Diffraction over the dimer showing the typical pattern of a single-crystal.

2.3 Unveiling the mechanism of nanocube epitaxy

A number of control experiments were carried out to establish the framework of nanocube epitaxy and shine light on the mechanism. Thermodynamics drives a system to lower its total free energy, which ultimately controls the equilibrium shape of nanostructures, although kinetic barriers have to be overcome in most circumstances. In the case of two almost touching, ligand-free nanocubes, the total free energy is reduced if the dimer welds in a continuous bar, as a result of the disappearance of two surfaces. However, from TEM analysis we observed that, on average, adjacent nanocubes were separated by a gap corresponding to $\sim 1x$ the lattice constant (corresponding to two atomic planes) that is sufficient to prevent spontaneous welding in water at RT, even after a few days (Figures S7).

In the previous section we hypothesized that two mechanisms were at play: heterogeneous nucleation on the nanocubes (growth) and oxidative etching.

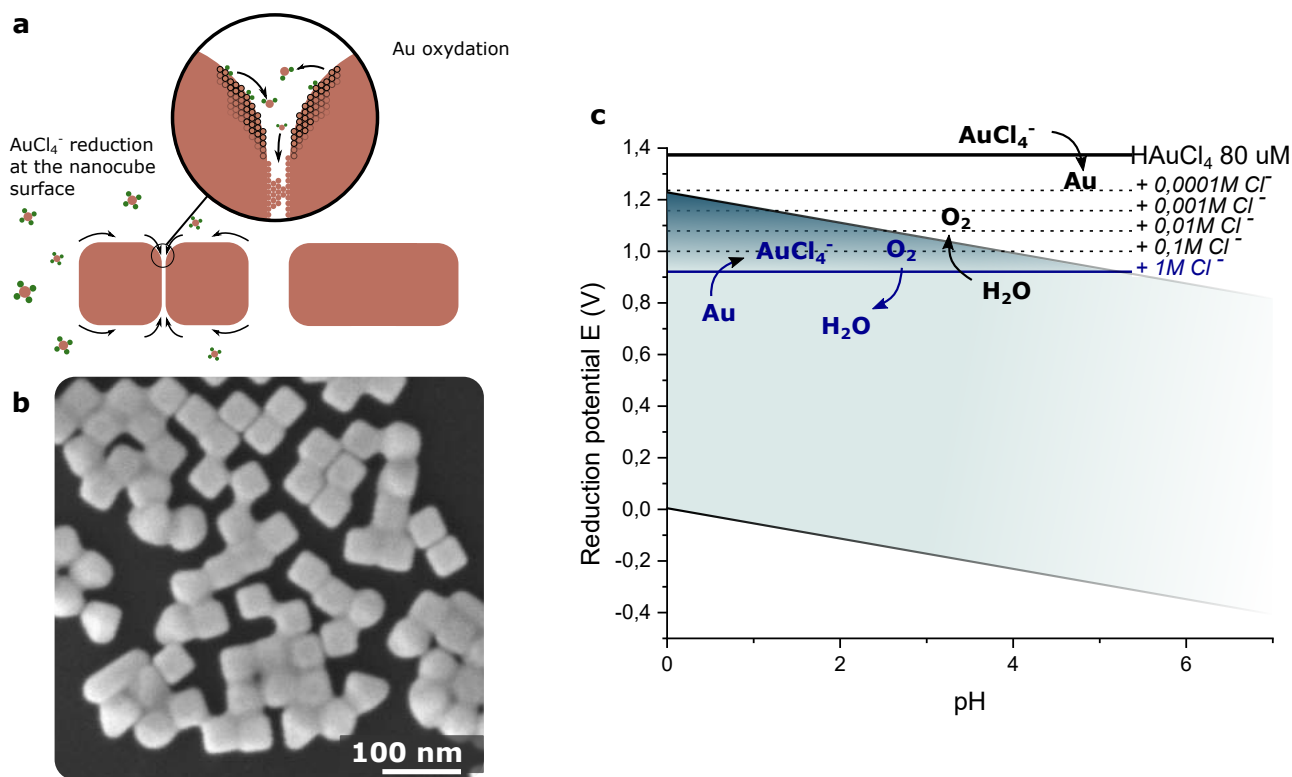


Figure 4: Insight into the welding mechanism. a) Illustration of the welding mechanism exhibiting simultaneous oxidation and growth. b) 38 nm gold nanocubes on silicon, partially welded using micromolar NaCl concentration only at 40°C . c) Pourbaix diagram of $\text{AuCl}_4^-/\text{Au}(0)$ redox couple for AuCl_4^- concentration of $80 \mu\text{M}$ at RT (black line). The green area shows the stability domain of water, while the dashed and blue line correspond to $\text{AuCl}_4^-/\text{Au}(0)$ reduction potential in the presence of chloride.

In Figure 4c we present the Pourbaix diagram to illustrate the thermodynamic equilibrium of the $\text{AuCl}_4^-/\text{Au}(0)$ redox couple as a function of pH in the absence of ligands (removed before welding). While there should be no stability domain for Au(III) species (AuCl_4^-) in our experimental conditions (black solid line), increasing Cl^- concentration and reducing pH can drive the system to a chemical equilibrium in which AuCl_4^- species are stable in solution, and therefore oxidative dissolution (corrosion) can take place. The strong binding affinity of chloride ions towards (111) and (110) facets [30] implies an enhanced reactivity of nanocube corners and edges towards oxidative dissolution. This is qualitatively validated with a set of experiments summarized in Figures S3, S4, S5, showing that rounding of nanocube corners is more pronounced at larger Cl^- concentration and lower pH. The apparent quantitative disagreement with the

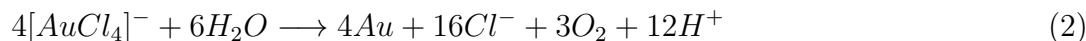
Pourbaix diagram can be explained by considering that, as a result of adsorption, the Cl^- concentration on the nanocube surface is substantially larger than in the bulk.

Studies on oxidative etching of gold nanoparticles in chlorinated solutions revealed that AuCl_2^- (Au(I)) was the main dissolution product [53, 54, 55]. It is however unstable at low temperature [56, 57] and can disproportionate to AuCl_4^- and Au(0) at the nanocube surface (Equation 1).



From the macroscopic point of view this would result in the displacement of Au atoms via chlorinated species intermediates. To test this hypothesis and identify the role of Cl^- , we replaced the 80 μM HAuCl_4 solution with a NaCl solution containing an equivalent concentration of free chloride (2.5 μM - calculations are detailed in the supporting material) and observed partial welding (Figure 4b). This suggests that gold atoms effectively migrate from (111) and (110) facets to (100) facets (including the gap) via dissolution in the presence of Cl^- ions and redeposition, as illustrated in Figure 4a. It is worth noticing that this mechanism is in agreement with the interpretation of the optical characterization results presented in Figure 2f. Nevertheless, we were not able to achieve complete welding while securing the shape of the nanocubes using NaCl only. Therefore, when performing nanocube epitaxy in the HAuCl_4 solution, part of the welding material is coming from the nanocubes but a fraction must come from the gold precursor. UV-Visible spectra performed on the welding solution after 1h at 40°C revealed a $\sim 2\text{x}$ larger Au(III) consumption in the presence of the nanocube substrate, corroborating our hypothesis (Figure S10).

According to the Pourbaix diagram, in our experimental conditions it is thermodynamically possible for water to reduce Au (III) directly to Au (0) (Equation 2), or to Au (I), that can be further reduced to Au (0) or can disproportionate following Equation 1 (Figure S20).



Although this seems in stark contrast with the fact that gold chloride aqueous solutions are typically stable in ambient conditions, the Pourbaix diagram does not take into account the kinetics of the system. Previous research has shown that in certain experimental conditions (aerosol microdroplets or microwave reactors), water oxidation could even lead to the formation of gold nanoparticles from HAuCl_4 solutions without reducing agents [4, 58].

In addition, we observed that in most experimental conditions the morphology of the nanostructures does not evolve after welding is complete, even if the substrate is left to react for longer time (Figure S11). This is the trademark of a self-limited reaction, and indicates that the equilibrium between oxidative etching and growth is reached once the gap has been filled.

2.4 Controlling the morphology

The accurate choice of experimental parameters allows to shift this equilibrium and favor dissolution or growth, providing a useful knob to finely control the morphology of the nanostructures resulting from nanocube epitaxy. Figure 5a summarizes some key parameters that can be tuned to design a specific surface and examples are given in Figure 5b, c and d for 42-nm nanocubes dropcasted onto silicon and exposed to the welding solution for 1h.

As discussed previously, chloride ions enhance oxidative dissolution and can be used to fabricate smooth nanostructures with important bending radius. However, as shown in Figure 5b, shape retention is very limited for large 2D nanocube assemblies.

Retention of sharp corners can be achieved by performing epitaxy at RT. However, in addition to the slow kinetics, many face-to-face nanocubes remained unwelded at the end of the reaction (Figure S6). This induced us to investigate the opportunity to control the evolution equilibrium between (100) and (111) facets by the introduction of Br^- ions at micromolar concentration to achieve flat surfaces even at higher temperature (Figure 5d). Bromine ions are commonly used in nanocube synthesis to direct crystal growth because they bind to (100) facets, reducing their surface energy and growth rate [28, 48].

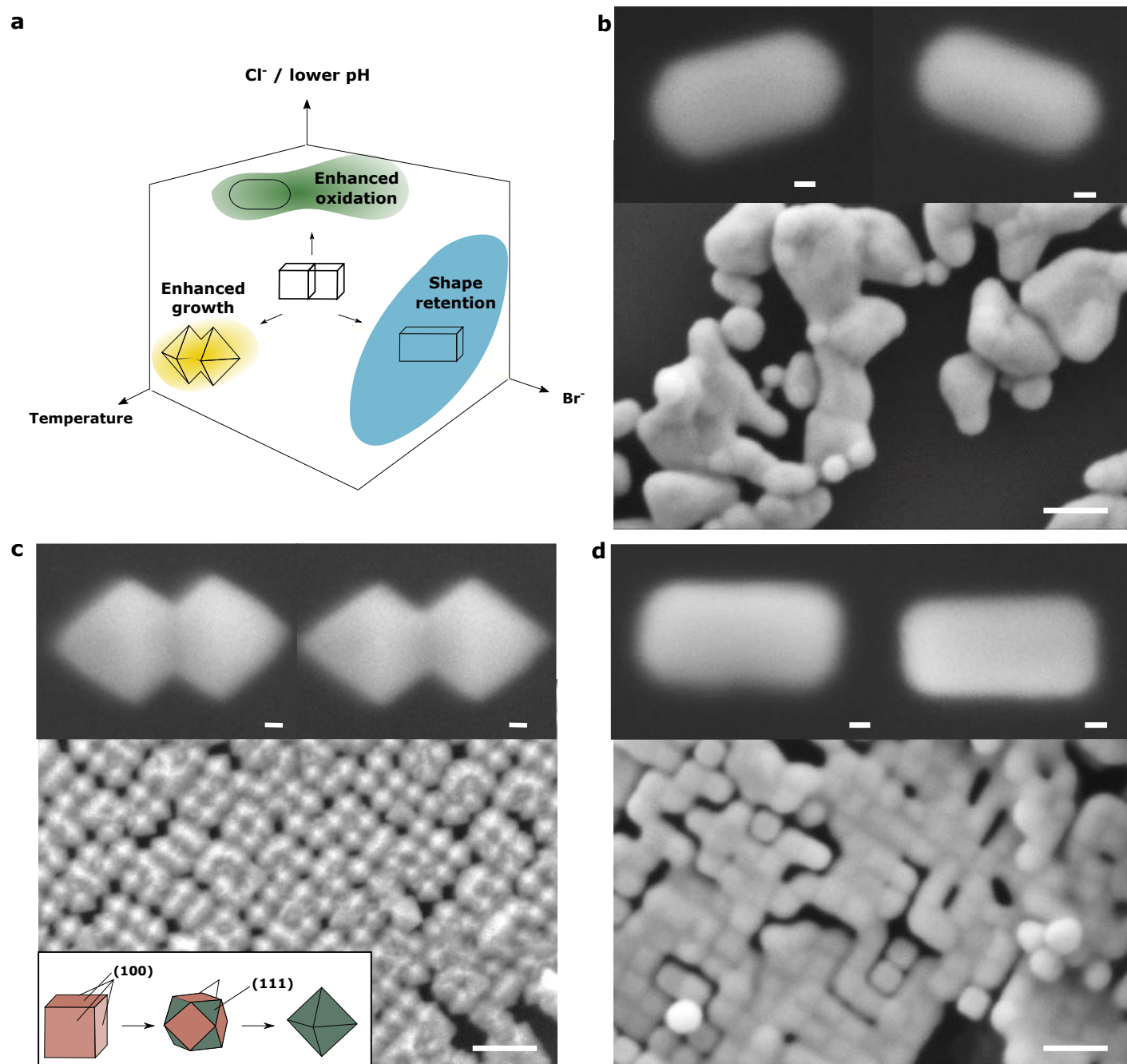


Figure 5: Control over the morphology. a) Schematic summary of the effect of experimental conditions on the nanostructure morphology. b) SEM images of gold nanocubes after welding for one hour in the presence of extra chloride ($80\mu\text{M}$ HAuCl_4 , $100\mu\text{M}$ NaCl , 40°C) to enhance oxidation dissolution. c) SEM images of gold nanocubes after welding for one hour at higher temperature ($80\mu\text{M}$ HAuCl_4 , 60°C) to promote overgrowth and the advent of egg-boxes structures made of (111) facets. The inset is a schematic representation of (100) capped nanocube reshaping into (111) capped octahedron. d) SEM images of gold nanocubes after welding for one hour in the presence of small quantities of NaBr ($80\mu\text{M}$ HAuCl_4 , $50\mu\text{M}$ NaBr , 40°C) to promote shape retention. The scale bar is 100 nm in the main images and 10 nm in the insets.

Increasing the temperature leads to rough morphologies, due to stronger heterogeneous nucleation as shown in Figure 5c. As the reaction temperature increases from RT to 40°C, nanostructures with irregular surfaces and egg-box shape start to appear after welding, exhibiting (111) facets. This effect is strengthened if the temperature is further increased to 60°C and 80°C (Figure S6). In the absence of surfactants or additives, the surface free energy of (111) facets is lower than that of (100) facets. This drives the reorganization of (100) capped nanostructures into (111) and their intermediates, as illustrated in the inset of Figure 5c. In addition, Figure 5c shows that only the surfaces that are not blocked by the substrate or the surrounding nanocubes are able to evolve towards (111) facets, and in the case of isolated dimers this results in the formation of bowties nanostructures. The larger volume after the reaction confirms that growth takes place on (100) facets exposed to the welding solution despite the absence of a reductant.

3 Conclusion

We have shown for the first time that gold monocrystalline nanostructure arrays of arbitrary shape could be fabricated via a bottom-up approach, using nanocubes as building blocks. This report challenges conventional approaches in the fields of plasmonics and crystal growths. In the former, focus is either put on the fabrication of plasmonic structures of average material quality with accurate control of the nanoscale geometry via top-down techniques, or on Platonic colloidal nanoparticles of high material quality enabled by low cost bottom-up chemical synthesis. In the latter, single crystal ingots are obtained from the melt using one single-crystal seed, whereas monocrystalline thin films are obtained via epitaxy in vacuum on substrates with the same lattice parameter. The results presented in this article represent a considerable step forward compared to the state of the art of these fields, and they have the potential to foster different research avenues. They show that monocrystalline gold nanostructures can be simply obtained via nanocube epitaxy at near ambient temperature from many single-crystal seeds (nanocubes) that could be assembled deterministically. This is especially important because the organisation of nanocubes before epitaxy determines the final shape of the monocrystalline nanostructure, allowing spatial resolution comparable to e-beam lithography, but with a process that has a strong potential from the technological perspective. The absence of a reducing agent during the nanocube epitaxy step simplifies the process substantially and avoids homogeneous nucleation of nanoparticles that would otherwise deteriorate the optical properties of the plasmonic surface. Optical measurements confirmed the excellent material quality and showed a strong reproducibility of process. In addition, unlike conventional nanofabrication techniques where the (polycrystalline) nanostructures are fabricated directly on the substrate, we have shown that nanocube epitaxy can be performed directly on PDMS and that (monocrystalline) plasmonic surfaces by-design can be printed to any substrate, unleashing from lattice matching requirements. This is highly promising for the integration of monocrystalline gold nanostructures, such as transparent electrodes or plasmonic scatterers, in devices that are sensitive to temperature, water or other nanofabrication processes, as for example perovskite solar cells. Detailed analysis of the chemical landscape and optical spectroscopy in operando shone light on the nanocube epitaxy mechanism, revealing that gold atoms are displaced from the nanocube corners to the sub-nanometer gap via a self-limited redox reaction mediated by Cl⁻ ions. Tuning this redox equilibrium allows to change the morphology of the nanostructures after epitaxy, transforming a nanocube dimer either into a continuous rectangular bar or into a bowtie element. The opportunity to configure the crystal facets during epitaxy widens the toolbox of geometries that can be achieved.

4 Experimental section

PDMS was purchased from Wacker (RT601), HAuCl₄, HNO₃, NaBr, NaCl, NaBH₄ were purchased from Merck at the highest purity available.

Gold Nanocube synthesis: Nanocubes were synthesized following Park et al. procedure [59]. Briefly, 10 nm CTAC-capped seeds were overgrown in a 50 mL round bottom flask using 6 mL of 100 mM CTAC, 30

μL of sodium bromide at 40 mM, 100 μL of the 10 nm seed solution at 2 OD in 20 mM CTAC, 390 μL 10 mM ascorbic acid and 6 mL of 0.5 mM HAuCl_4 solution. The solution was left to react for 25 minutes at RT with gentle stirring prior to centrifugation. The nanocube solution was washed twice and redispersed in 10 mL of ultrapure water.

Ligands removal: Ligands are removed after nanocubes are supported on a substrate (dropcasted on a flat substrate such as silicon or assembled into patterned PDMS). The substrate is first dipped (sequentially) in ultrapure water, acetone, isopropanol and ultrapure water again (one minute each) to have the substrate as clean as possible before ligand desorption. The ligands adsorbed on the nanocube surface (CTAC, SDS, Triton-X45 residual from the synthesis or the assembly solution) are removed by exposing the substrate to a 100 mM NaBH_4 solution for 30 minutes. Hydrides having a higher binding affinity to gold effectively displace the ligands, as reported in ref. [42]. Finally, the samples are rinsed thoroughly with ultrapure water and stored in ultrapure water until welding.

Nanocube epitaxy on silicon: Typically 2 μL of an aqueous nanocube solution (10^{12} nanocubes/mL) is dropcasted on a silicon substrate. Ligands are always removed after complete evaporation of the solution with the procedure described above. Welding was performed by introducing the silicon substrate into a 20 mL vial containing 10 mL of a HAuCl_4 aqueous solution with concentrations ranging from 1 μM to 10 mM, at a temperature between RT and 80°C between 1 second and one hour using a water bath, with no agitation. The standard welding reaction on silicon was performed at 40°C with 80 μM HAuCl_4 unless mentioned otherwise. When NaCl, NaBr, NaOH, HCl and HNO_3 are added to control the shape of the nanostructures, the concentrations and/or measured pH are systematically indicated in the main text or figure captions. After welding the substrates were rinsed with ultrapure water and N_2 dried.

PDMS molds fabrication: The silicon master was fabricated with e-beam lithography using PMMA resist on silicon. Upon exposition and development, a thin layer of chrome was evaporated on the substrate to be used as a hardmask. PMMA was then lifted-off in acetone. Silicon was then etched by 40 nm using Reactive Ion Etching (RIE). Chrome was finally removed using a commercial chrome etchant. After oxygen plasma, the silicon master was silanized with perfluorodecyltrichlorosilane at room temperature in a desiccator for 20 minutes to ease PDMS demolding. PDMS moulds were fabricated on a glass slide by depositing liquid degassed PDMS (commercial monomer and polymerizing agent mixed to a 9:1 ratio) on the silicon master and covering it by a glass slide. Upon reticulation of PDMS at 100°C for 10 minutes on a hot plate, the PDMS template was demolded from the silicon master. The PDMS moulds were then stored in ethanol for at least a few days prior to assembly to remove un-reacted species in PDMS.

Capillary assembly: The nanocube solution was centrifuged at 9,000 RPM for 10 minutes and redispersed in 10 mL of 0.75 mM SDS and 0.0075 wt.% Triton X45 at a concentration of 10^{12} nanocubes/mL. Assembly was performed by dragging the nanocube solution (50 μL) with a glass slide fixed 1 mm above the PDMS substrate, in a home-made system. The speed was set at $1 \mu\text{m}\cdot\text{s}^{-1}$, the temperature at 55°C and the humidity at 40% [45].

Nanocube epitaxy on PDMS: Assemblies were left to fully dry in air for at least an hour before removing the ligands with the strategy described above (when dipping the samples in NaBH_4 right after assembly, part of the assembly would come off the substrate). Welding was performed by introducing the PDMS substrate into a solution containing 80 μM HAuCl_4 , 50 μM NaBr and 100 μL of HNO_3 to lower the pH to 1. Reaction was performed at 40°C for one hour, with no agitation. Upon welding substrates were rinsed with ultrapure water and dried with a stream of nitrogen.

Printing: Printing was performed on silicon substrates and Si_3N_4 TEM grids, used as the receiving substrates. For silicon substrate, an oxygen plasma (10 minute, 200W, 150°C) was first performed, then 5 μL

of ethanol was dropcasted on the substrate at 20°C and the PDMS sample was slowly put in contact and pressed on the silicon substrate before evaporation of the ethanol. The whole process was monitored using optical microscope by looking through the transparent PDMS, to ensure for good contact between the two substrates and to position assembled areas on silicon. When the two substrates were fully in contact, the temperature was then raised and maintained at 50°C for 10 minutes for the ethanol to dry. Upon releasing the pressure nanocubes remained in the silicon for which they have more affinity. The Si₃N₄ TEM grids were used as purchased without plasma treatment. Because they cannot handle much pressure without breaking, 1 μL of PMMA was deposited on the TEM grids to increase their adhesion, which allowed to print the nanocube assemblies with good resolution. Upon contact with PDMS, PMMA was pushed out of the sample which allowed imaging.

Characterization and simulations: Assemblies of nanocubes on PDMS were imaged using a scanning electron microscope (JEOL 7900F) in low vacuum mode with a pressure of 60 Pa. TEM and electron diffraction was performed with a JEOL 2100F. Optical characterisation was performed with an inverted microscope (Zeiss Axiovert 200M) with an air objective (100X, NA = 0.9) in reflection. The PDMS without nanoantennas was used as the reference to take into account of the spectral response of the system. Light was coupled into a 25 μm optical fiber, yielding a collection spot diameter of 1.3 μm. To minimize perturbation of the nanoreactors during *Operando* measurements, spectra were taken at discreet intervals: the first 15 spectra were collected each 30 s, the following 5 spectra each 60 s, and the last 4 spectra each 4 minutes.

The commercial software Lumerical was used to simulate the response of individual gold nanoantennas. The nanostructure was placed on PDMS to simulate the experimental environment as accurately as possible, as depicted in Figure S17d. A total field scattered field source (electric field polarized along the nanoantenna long axis) was used in all simulations, except in Figure S18, where a periodic array with lattice parameters equivalent to experiments was simulated. In Figure 2d the following nanostructure dimensions were used: $w = 44$ nm, $L = 84$ nm, $r = 8$ nm. The dielectric constant from Johnson and Christy was used for gold.

To fully understand how the far-field optical response changes, one has to consider that the dimers before welding are separated by a gap < 0.5 nm (measured by TEM and presented in Figure S14 - middle panel). In this regime, electron tunnelling dominates the optical response. The gap can thus be considered as an element with a given (small) impedance. The establishment of a bridge between the two nanocubes and its widening effectively reduce the gap impedance further and increase the plasmonic current in the gap. The increased current improves the cross-section of the resonator. This has, however, a negligible effect on the resonance position, given that the optical mode before welding corresponds already to that of a continuous dimer (due to electron tunnelling) and the effective length of the resonator is virtually unchanged as the gap is filled. This is consistent with theoretical predictions for flat interfaces reported in [49] and [50]. It is worth mentioning that this particular behaviour is strongly dependent on the morphology of the gap, as shown in theoretical and numerical studies of plasmonic dimers of different shapes. In particular in [49] it is shown that gaps constituted by flat interfaces display strikingly different behaviour than those constituted by spherical interfaces.

Statistical analysis: The information given on width, length, radius of curvature of nanocubes and nanostructures, as well as the size of the gap between two nanocubes (before welding) are extracted from manual measurements performed on TEM images. Mean values are indicated with standard deviation (SD) calculated for: (i) 6 values for the bending radius of dimers and individual nanocubes, (ii) 11 values for the size of the gap between two nanocubes, and (iii) 8 values for the width and length of the dimers before and after welding. All the measures are presented in Figure S14.

Supporting Information

Supporting Information is available from the Wiley Online Library or from the author.

Acknowledgements

The authors thanks M. Abbarchi and L. Santinacci for fruitful discussions and for carefully reading the paper, D. Chaudanson and A. Altié for support with TEM characterisation and F. Bedu for support with e-beam lithography. B. Sciacca thanks AMUtech, MITI CNRS (project COMPACT) and ANR (project MeMeNtO) for funding.

References

- [1] E. C. Garnett, B. Ehrler, A. Polman, E. Alarcon-Llado, *ACS Photonics* **2021**, *8*, 1 61.
- [2] A. F. Koenderink, A. Alù, A. Polman, *Science* **2015**, *348*, 6234 516.
- [3] J. H. Choi, H. Wang, S. J. Oh, T. Paik, P. S. Jo, J. Sung, X. Ye, T. Zhao, B. T. Diroll, C. B. Murray, C. R. Kagan, *Science* **2016**, *352*, 6282 205.
- [4] J. K. Lee, D. Samanta, H. G. Nam, R. N. Zare, *Nature Communications* **2018**, 1–9.
- [5] S. a. Maier, *Fundamentals and Applications Plasmonics : Fundamentals and Applications*, **2007**.
- [6] M. S. Bin-Alam, O. Reshef, Y. Mamchur, M. Z. Alam, G. Carlow, J. Upham, B. T. Sullivan, J. M. Ménard, M. J. Huttunen, R. W. Boyd, K. Dolgaleva, *Nature Communications* **2021**, *12*, 1 974.
- [7] K. L. Kelly, E. Coronado, L. L. Zhao, G. C. Shatz, *Journal of Physical Chemistry B* **2003**, *107* 668.
- [8] R. Keunen, D. MacOretta, N. Cathcart, V. Kitaev, *Nanoscale* **2016**, *8*, 5 2575.
- [9] S. Eustis, M. A. El-Sayed, *Chemical Society Reviews* **2006**, *35*, 3 209.
- [10] G. Baffou, R. Quidant, *Chemical Society Reviews* **2014**, *43*, 11 3898.
- [11] Q. Shi, T. U. Connell, Q. Xiao, A. S. Chesman, W. Cheng, A. Roberts, T. J. Davis, D. E. Gómez, *ACS Photonics* **2019**, *6*, 2 314.
- [12] S. Nie, S. R. Emory, *Science* **1997**, *275*, 5303 1102.
- [13] K. A. Willets, R. P. Van Duyne, *Annual Review of Physical Chemistry* **2007**, *58* 267.
- [14] J. Nuñez, A. Boersma, J. Grand, S. Mintova, B. Sciacca, *Advanced Functional Materials* **2021**, *31*, 24 2101623.
- [15] E. Cortés, W. Xie, J. Cambiasso, A. S. Jermyn, R. Sundararaman, P. Narang, S. Schlücker, S. A. Maier, *Nature Communications* **2017**, *8* 14880.
- [16] M. Navlani-García, D. Salinas-Torres, K. Mori, Y. Kuwahara, H. Yamashita, *Catalysis Surveys from Asia* **2019**, *23*, 3 127.
- [17] S. Linic, U. Aslam, C. Boerigter, M. Morabito, *Nature Materials* **2015**, *14*, 6 567.
- [18] J. N. Anker, W. P. Hall, O. Lyandres, N. C. Shah, J. Zhao, R. P. V. Duyne, *Nature Materials* **2008**, *7* 442–.
- [19] X. Yang, M. Yang, B. Pang, M. Vara, Y. Xia, *Chemical Reviews* **2015**, *115*, 19 10410.
- [20] H. A. Atwater, A. Polman, *Nature Materials* **2010**, *9*, 3 205.
- [21] E. Oksenberg, I. Shlesinger, A. Xomalis, A. Baldi, J. J. Baumberg, A. F. Koenderink, E. C. Garnett, *Nature Nanotechnology* **2021**.
- [22] R. Won, *Nature Photonics* **2017**, *11*, 8 462.
- [23] A. Biswas, I. S. Bayer, A. S. Biris, T. Wang, E. Dervishi, F. Faupel, *Advances in Colloid and Interface Science* **2012**, *170* 2.

- [24] Y. Wu, C. Zhang, N. M. Estakhri, Y. Zhao, J. Kim, M. Zhang, X.-X. Liu, G. K. Pribil, A. Alù, C.-K. Shih, X. Li, Advanced Materials **2014**, *26*, 35 6106.
- [25] A. Capitaine, B. Sciacca, Advanced Materials **2021**, n/a, n/a 2102588.
- [26] P. Nagpal, N. C. Lindquist, S.-H. Oh, D. J. Norris, Science **2009**, *325*, 5940 594.
- [27] H. Zhang, C. Kinnear, P. Mulvaney, Advanced Materials **2020**, *32*, 18 1904551.
- [28] J. E. Park, Y. Lee, J. M. Nam, Nano Letters **2018**, *18*, 10 6475.
- [29] J. J. D. Yoreo, P. U. P. A. Gilbert, N. A. J. M. Sommerdijk, R. L. Penn, S. Whitelam, D. Joester, H. Zhang, J. D. Rimer, A. Navrotsky, J. F. Banfield, A. F. Wallace, F. M. Michel, F. C. Meldrum, H. Cölfen, P. M. Dove, Science **2015**, *349*, 6247 aaa6760.
- [30] J. E. Millstone, W. Wei, M. R. Jones, H. Yoo, C. A. Mirkin, Nano Letters **2008**, *8*, 8 2526.
- [31] B. Sciacca, A. Berkhout, B. J. Brenny, S. Z. Oener, M. A. van Huis, A. Polman, E. C. Garnett, Advanced Materials **2017**, *29*, 26 1701064.
- [32] H. J. Yang, S. Y. He, H. L. Chen, H. Y. Tuan, Chemistry of Materials **2014**, *26*, 5 1785.
- [33] B. D. Clark, C. R. Jacobson, M. Lou, D. Renard, G. Wu, L. Bursi, A. S. Ali, D. F. Swearer, A. L. Tsai, P. Nordlander, N. J. Halas, ACS Nano **2019**, *13*, 8 9682.
- [34] Y. Wang, Y. Zheng, C. Z. Huang, Y. Xia, Journal of the American Chemical Society **2013**, *135*, 5 1941.
- [35] C. H. Kuo, C. H. Chen, M. H. Huang, Advanced Functional Materials **2007**, *17*, 18 3773.
- [36] H. S. Chen, S. C. Wu, M. H. Huang, Dalton Transactions **2014**, *44*, 34 15088.
- [37] M. Imran, P. Ijaz, D. Baranov, L. Goldoni, U. Petralanda, Q. Akkerman, A. L. Abdelhady, M. Prato, P. Bianchini, I. Infante, L. Manna, Nano Letters **2018**, *18*, 12 7822.
- [38] F. Dang, K. I. Mimura, K. Kato, H. Imai, S. Wada, H. Haneda, M. Kuwabara, CrystEngComm **2011**, *13*, 11 3878.
- [39] U. A. Joshi, J. S. Jang, P. H. Borse, J. S. Lee, Applied Physics Letters **2008**, *92*, 24 2006.
- [40] S. Yang, L. Gao, Journal of the American Chemical Society **2006**, *128*, 29 9330.
- [41] M. Haggui, M. Dridi, J. Plain, S. Marguet, H. Perez, G. C. Schatz, G. P. Wiederrecht, S. K. Gray, R. Bachelot, ACS Nano **2012**, *6*, 2 1299.
- [42] S. M. Ansar, F. S. Ameer, W. Hu, S. Zou, C. U. Pittman, D. Zhang, Nano Letters **2013**, *13*, 3 1226.
- [43] S. Ni, J. Leemann, I. Buttinoni, L. Isa, H. Wolf, Science Advances **2016**, *2*, 4 e1501779.
- [44] V. Flauraud, M. Mastrangeli, G. D. Bernasconi, J. Butet, D. T. Alexander, E. Shahrabi, O. J. Martin, J. Brugger, Nature Nanotechnology **2017**, *12*, 1 73.
- [45] T. Kraus, L. Malaquin, H. Schmid, W. Riess, N. D. Spencer, H. Wolf, Nature Nanotechnology **2007**, *2*, 9 570.
- [46] L. Malaquin, T. Kraus, H. Schmid, E. Delamarche, H. Wolf, Langmuir **2007**, *23*, 23 11513.
- [47] S. Ni, L. Isa, H. Wolf, Soft Matter **2018**, *14*, 16 2978.
- [48] M. E. King, I. A. Kent, M. L. Personick, Nanoscale **2019**, *11* 15612.
- [49] R. Esteban, G. Aguirregabiria, A. G. Borisov, Y. M. Wang, P. Nordlander, G. W. Bryant, J. Aizpurua, ACS Photonics **2015**, *2*, 2 295.

- [50] D. Knebl, A. Hörl, A. Trügler, J. Kern, J. R. Krenn, P. Puschnig, U. Hohenester, Phys. Rev. B **2016**, 93 081405.
- [51] M. H. Oh, M. G. Cho, D. Y. Chung, I. Park, Y. P. Kwon, C. Ophus, D. Kim, M. G. Kim, B. Jeong, X. W. Gu, J. Jo, J. M. Yoo, J. Hong, S. McMains, K. Kang, Y.-E. Sung, A. P. Alivisatos, T. Hyeon, Nature **2020**, 577, 7790 359.
- [52] R. G. Mariano, K. McKelvey, H. S. White, M. W. Kanan, Science **2017**, 358, 6367 1187.
- [53] S. Yoon, C. Kim, B. Lee, J. H. Lee, Nanoscale Adv. **2019**, 1 2157.
- [54] S. Seisko, M. Lampinen, J. Aromaa, A. Laari, T. Koiranen, M. Lundström, Minerals Engineering **2018**, 115, October 2017 131.
- [55] M. J. Nicol, Gold Bulletin **1980**, 13, 3 105.
- [56] J. A. Peck, C. D. Tait, B. I. Swanson, G. E. Brown, Geochimica et Cosmochimica Acta **1991**, 55, 3 671.
- [57] C. H. Gammons, Y. Yu, Geochimica et Cosmochimica Acta **1997**, 61, 10 1971.
- [58] C. Vargas-Hernandez, M. M. Mariscal, R. Esparza, M. J. Yacaman, Applied Physics Letters **2010**, 96 2013115.
- [59] Colloids and Surfaces A: Physicochemical and Engineering Aspects **2018**, 558, June 186.
- [60] L. Sun, Y. Chen, F. Gong, Q. Dang, G. Xiang, L. Cheng, F. Liao, M. Shao, Journal of Materials Chemistry B **2019**, 7, 28 4393.
- [61] A. Usher, D. C. Mcphail, Geochimica et Cosmochimica **2009**, 73 3359.